Progress In Electromagnetics Research C, Vol. 117, 185–201, 2021

Frequency Diverse ISAR Two-Dimensional Imaging Method and Resolution Analysis

Xiu-Ping Li[1], Ke-Fei Liao[1, *], and Bo Wen[2]

Abstract—Aiming at the shortcomings of complex broadband transmitter/receiver systems and inflexible bandwidth control in the existing inverse synthetic aperture radar (ISAR) imaging systems, in this paper, a novel two-dimensional imaging method based on frequency diverse ISAR (FDISAR) is proposed by combining frequency diversity technique with inverse synthetic aperture technique. In the imaging process, FDISAR is different from the stepped-frequency ISAR, which needs to transmit the same burst at different observation moments. Once the bandwidth is determined, the bandwidth of the subsequent burst synthesis cannot be changed, which reduces the flexibility of the radar system. In this method, single-frequency signals of different frequencies are transmitted to the target at different observation times, and the wideband signals are synthesized using the frequencies at different observation times to obtain the resolution capability in the range direction. In addition, the relative motion synthetic aperture of the target and radar is used to obtain the azimuth resolution capability, and finally the two-dimensional imaging capability of the moving target is formed. Specifically, we established an ISAR imaging model based on frequency diversity to synthesize a broadband signal and used an improved backward projection algorithm (BP) to complete the two-dimensional imaging of the target. On this basis, the influence of the transmission signal frequency selection on the imaging quality is analyzed, and the half-power resolution in range and azimuth directions is derived. Furthermore, in order to eliminate side lobes and improve imaging quality, we combined compressive sensing (CS) theory with a BP imaging algorithm based on compressed sensing to obtain high-quality target 2D images. Simulation and actual measurement results show that FDISAR can achieve two-dimensional imaging of moving multi-scattering point targets. The application of this method is of great significance for reducing the complexity of the ISAR imaging system and improving the flexibility of the system's control bandwidth resources.

1. INTRODUCTION

Inverse synthetic aperture radar imaging technology can carry out long-distance two-dimensional imaging of air targets in all weather, and is an extremely important technical means in modern battlefield defense systems [1–4]. In order to obtain high resolution in the range direction, ISAR imaging system usually transmits broadband chirp signal [5–8] or stepped-frequency signal [9, 10]. A series of imaging algorithms have been proposed for radar systems that transmit broadband chirp signals. Common imaging methods include range-Doppler algorithm [11], range instantaneous Doppler algorithm [12–14], super-resolution ISAR imaging algorithm [15], and ISAR imaging algorithm based on compressed sensing [16, 17]. However, these imaging algorithms proposed for radar systems with chirp signal modality can only improve the range resolution by increasing the transmitted signal bandwidth, which increases the complexity and cost of the radar system's transmitter and receiver [18]. At the

Received 12 October 2021, Accepted 28 December 2021, Scheduled 4 January 2022

* Corresponding author: Kefei Liao (kefeiliao@guet.edu.cn).

[1] School of Information and Communications, Guilin University of Electronic Technology, Guilin 541004, China. [2] The 54th Research Institute of China Electronics Technology Group, Shijiazhuang 050000, China.

same time, ISAR imaging technology is often applied to phased array radar systems. When the phased array transmits broadband signals, it will cause antenna beam pointing deviation and time dispersion effect, which needs to be solved by adopting a real-time delay phase shifter at each unit or sub-array level of the array [19], which will increase the hardware requirements of the system.

Compared with the radar system of chirp modality, the radar imaging system of stepped-frequency system has lower hardware requirements for high-resolution imaging, low instantaneous receiving bandwidth, and low AD sampling rate. These advantages make it of high engineering and practical value. A series of imaging algorithms have also been proposed for this system [20–22]. The intelligentization of radar, cognitive imaging, intelligent task planning, intelligent management, and optimized scheduling of radar resources all put forward higher requirements for the flexibility of resource control [23]. However, once the frequency step length of the stepped-frequency system radar and the number of sub-pulses in the burst are determined, the bandwidth and number of sub-pulses emitted cannot be adjusted during the imaging process, which makes it difficult to meet the imaging quality requirements of different targets. Therefore, the establishment of a set of flexible bandwidth control and low hardware requirements of the radar signal system, and under the system to propose the corresponding imaging methods to improve the intelligence of the radar imaging system is of great significance.

The frequency diverse array (FDA) technology can combine the single frequency signal emitted by a single array element to synthesize the broadband signal [24, 25]. Applying the idea of frequency diversity to ISAR, the frequency diversity in space is transformed into the frequency diversity in time to form a new FDISAR system. In this system, the radar only needs to transmit a single frequency signal at each observation time. The broadband signal is synthesized by superposing the echo signals of different frequencies emitted at different observation moments, and synthetic aperture is generated by combining the relative motion between the target and the radar, finally forming the two-dimensional resolution capability of the target. The advantages of this technology are mainly as follows:

A. it does not need to transmit broadband signals, which will reduce the requirements of radar transmitter and receiver;

B. it can flexibly adjust the signal bandwidth by increasing or decreasing the number of transmitted signal frequencies, which is conducive to resource allocation according to target characteristics and improves the intelligence of radar system [23].

This paper will study the imaging method of FDISAR, the influence of frequency selection on imaging quality, and the derivation of resolution.

This paper is organized as follows. The signal model of FDISAR imaging is presented in Section 2. The improved backward projection algorithm, periodic analysis of imaging results, and resolution derivation are given in Section 3. In addition, in order to further improve the imaging quality, a BP imaging algorithm based on compressed sensing is proposed. Simulated and measured data-based experimental results are analyzed in Section 4. The conclusion is given in Section 5.

2. SIGNAL MODEL

This article is mainly aimed at the target of smooth motion, that is, the target can be regarded as a uniform linear motion during the imaging process. Therefore, the geometric relationship between the target and radar during the FDISAR imaging process is shown in Fig. 1.

It can be seen from the signal model that unlike the stepped frequency signal ISAR system, the FDISAR system transmits narrowband signals $f_1, f_2 ... f_n$ of different frequencies at different times $t_1, t_2 ... t_n$, and does not repeat these narrowband signals. Therefore, FDISAR has the flexibility to adjust the bandwidth by transmitting narrowband signals of different frequencies. Through the algorithm synthesis in the later stage, the broadband observation effect can be obtained.

For the convenience of analysis, the target's motion model is decomposed into translational and rotational components. FDISAR imaging geometry diagram is shown in Fig. 2.

At the initial moment, the origins of the target moving coordinate axis x-y and the fixed coordinate axis v-u are the same point, and the angle between the coordinate axes is θ_0. The relationship between the target motion coordinate axis and the fixed coordinate axis can be rewritten as:

$$\begin{bmatrix} u \\ v \end{bmatrix} = \begin{bmatrix} \cos[\theta(t)] & \sin[\theta(t)] \\ -\sin[\theta(t)] & \cos[\theta(t)] \end{bmatrix} \begin{bmatrix} y \\ x \end{bmatrix} + \begin{bmatrix} 0 \\ d(t) \end{bmatrix} \tag{1}$$

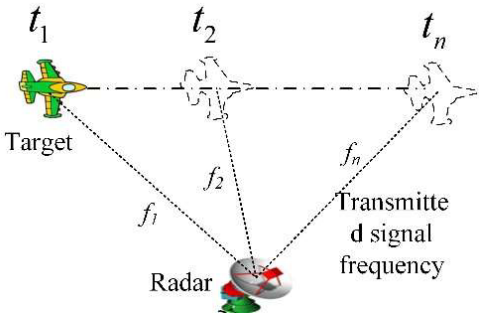

Figure 1. Geometric diagram of target and radar during imaging.

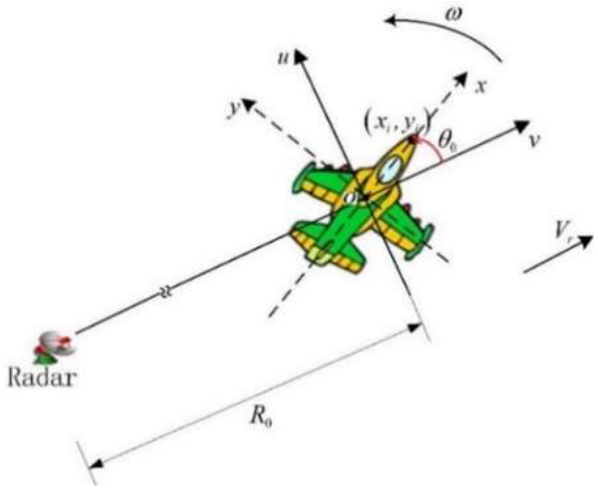

Figure 2. FDISAR imaging geometry diagram.

where $\theta(t) = \theta_0 + \omega t$ is the angle that the target has turned during the imaging process; ω is the speed at which the target rotates; $d(t) = V_r t$ is the distance that the target moves radially. The radar transmits single-frequency signals to the target at a certain time interval (T_{PRI} of pulse repetition interval). The frequency of the radar at the time of $t_n = nT_{\mathrm{PRI}}$ is $f_n = f_0 + f(n)$, $n = 1, 2, ...N$, f_0 is the starting frequency, and $f(n)$ is the signal frequency increment. Assuming that in the imaging process, the target is always in the radar beam, and there is no multiple scattering and no effect on polarization, then the echo signal received is as:

$$s_r(t, t_n) = \int_x \int_y I(x, y)\, s_t(t - 2R(t_n)/c)\, dxdy \tag{2}$$

where $I(x, y)$ is the scattering point function of the target; c is the speed of light; $R(t_n) = \sqrt{(R_0 + v(t_n))^2 + (u(t_n))^2}$ is the distance from the target to the radar; $v(t_n)$ and $u(t_n)$ can be represented by Equation (1). In the case of high frequency, the target can be regarded as a scattering point model, and the scattering point intensity of the target is assumed to be 1. At time t_n, the radar's transmitted signal is $s_t(t_n, t) = \mathrm{rect}(t/\tau)\exp(j2\pi f_n t)$, and τ is the pulse width. After mixing the received echo signal with $\exp(j2\pi f_n t)$, the echo signal can be expressed as:

$$s_r(t_n) = \sum_{i=1}^{I} \exp\left(-j2\pi f_n \frac{2R_i(t_n)}{c}\right) \tag{3}$$

where I is the number of scattering points, and $R_i(t_n)$ is the distance from the ith scattering point to the radar at time t_n.

3. BACKWARD PROJECTION ALGORITHM

Firstly, an improved backward projection algorithm based on two-dimensional coherent accumulation after phase compensation is introduced. Then the effect of linear frequency increment and random frequency multiplication increment on image quality is analyzed. In addition, the expression of half-power resolution is derived. Finally, BP imaging algorithm based on compressed sensing is proposed to improve the image quality.

The BP algorithm presented in this section is different from the traditional BP algorithm in that it does not need pulse compression, but directly obtains the coherence at the scattering point of the echo signal through phase compensation, and then carries out phase-coherent accumulation to obtain the two-dimensional image of the target. Since this paper is aimed at the target of smooth movement, it is

easy to obtain the target's movement trajectory, which ensures that the grid divided at each moment is completely matched.

3.1. Imaging Method

The BP algorithm in this paper is improved on the basis of the traditional BP algorithm and directly performs coherent accumulation on signals of different frequencies without distance compression. After the radar emits pulses, the grid is divided at a certain interval in the imaging area, and it is assumed that the grid divided at each moment exactly matches the target. By calculating the distance of each grid node from the radar, a phase compensation matrix with different distance histories is constructed. The schematic diagram of the grid division of the imaging area is shown in Fig. 3.

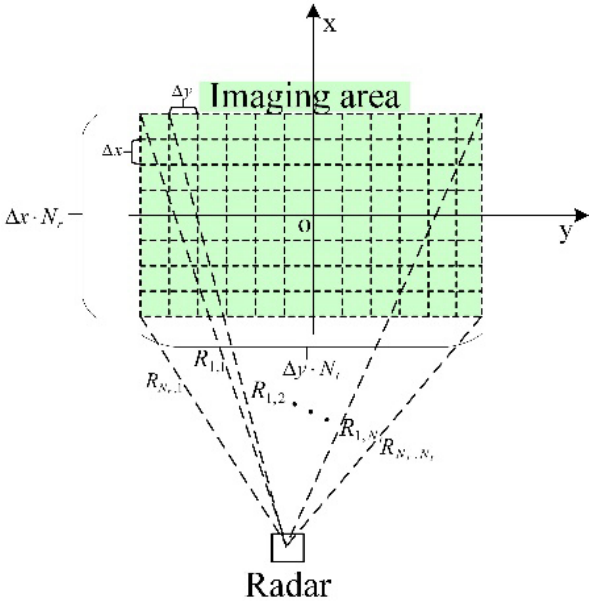

Figure 3. Schematic diagram of imaging area grid division.

Where, Δy is the spacing of grid division in the y-axis direction; Δx is the spacing of grid division in the x-axis direction; N_t is the total number of grid division in the y-axis direction; N_r is the total number of grid division in the x-axis direction; $R_{1,1}$ is the distance between grid node $(1,1)$ and the radar, and the phase compensation term on this node as: $e^{j2\pi f\frac{2R_{1,1}}{c}}$. Then the phase compensation matrix on the whole grid at time t_n can be expressed as:

$$\mathbf{\Theta}_{t_n} = \begin{bmatrix} e^{j2\pi f_n\frac{2R_{1,1}(t_n)}{c}} & e^{j2\pi f_n\frac{2R_{1,2}(t_n)}{c}} & \cdots & e^{j2\pi f_n\frac{2R_{1,Nt}(t_n)}{c}} \\ e^{j2\pi f_n\frac{2R_{2,1}(t_n)}{c}} & e^{j2\pi f_n\frac{2R_{2,2}(t_n)}{c}} & \cdots & e^{j2\pi f_n\frac{2R_{2,Nt}(t_n)}{c}} \\ \vdots & \vdots & \ddots & \vdots \\ e^{j2\pi f_n\frac{2R_{Nr,1}(t_n)}{c}} & e^{j2\pi f_n\frac{2R_{Nr,2}(t_n)}{c}} & \cdots & e^{j2\pi f_n\frac{2R_{Nr,Nt}(t_n)}{c}} \end{bmatrix}_{Nr\times Nt} \tag{4}$$

where the distance between grid node (nr, nt) and the radar is $R_{nr,nt}(t_n)=\sqrt{(R_0+v_{nr}(t_n))^2+(u_{nt}(t_n))^2}$. According to Equation (1), $v_{nr}(t_n)$ and $u_{nt}(t_n)$ can be obtained as follows:

$$\begin{bmatrix} u_{nt}(t_n) \\ v_{nr}(t_n) \end{bmatrix} = \begin{bmatrix} \cos[\theta(t_n)] & \sin[\theta(t_n)] \\ -\sin[\theta(t_n)] & \cos[\theta(t_n)] \end{bmatrix} \cdot \begin{bmatrix} (nt-([Nt/2]))\cdot\Delta y \\ (nr-([Nr/2]))\cdot\Delta x \end{bmatrix} + \begin{bmatrix} 0 \\ d(t_n) \end{bmatrix} \tag{5}$$

where $[\cdot]$ in $[Nt/2]$ and $[Nr/2]$ represents the down round operation. Echo matrix $\mathbf{E}_{t_n} = s_r(t_n)\cdot\mathbf{\Theta}_{t_n}$ is obtained by multiplying the echo signal at t_n time with the corresponding phase compensation matrix.

Then, the echo matrix of N times observation is added to realize the coherent accumulation of both distance direction and azimuth direction at the same time. Finally, the target two-dimensional image can be expressed as:

$$\mathbf{S} = \left| \sum_{n=1}^{N} \mathbf{E}_{t_n} \right| \tag{6}$$

3.2. Periodic Analysis of Imaging Results

This section mainly analyzes the effect of linear frequency increment and random frequency multiplication increment on imaging results. The phase compensation is carried out for the echo signal of any scattering point i falling on the grid node in Fig. 3. Then the result of phase-coherent accumulation of echo data after N times of phase compensation can be expressed as:

$$S_R(nr, nt) = \sum_{n=1}^{N} \exp\left(j2\pi f_n \left(2\,\frac{R_{nr,nt}(t_n) - R_i(t_n)}{c} \right) \right) \tag{7}$$

Suppose that the initial angle between coordinate axes is $\theta_0 = 0$. In general, the angle that the target turns relative to the radar during the imaging process satisfies: $\omega t < 5^\circ$. Then the angle can be regarded as a small corner,

$$R_i(t_n) \approx R_0 + x_i - y_i \cdot \omega t_n + V_r t_n \tag{8}$$

$$R_{nr,nt}(t_n) \approx R_0 + x_{nr} - y_{nt} \cdot \omega t_n + V_r t_n \tag{9}$$

where $x_{nr} = (nr - ([Nr/2])) \cdot \Delta x$, $y_{nt} = (nt - ([Nt/2])) \cdot \Delta y$, $\omega t_n = n \cdot \Delta\theta$. $\Delta\theta = T_{\mathrm{PRI}} \cdot \omega$ is the rotation angle of the target within a transmitting signal interval (ω is a constant), and then Equation (7) can be simplified as:

$$\begin{aligned} S_R(nr, nt) &= \sum_{n=1}^{N} \exp\left(j2\pi f_n \left(2\frac{x_{nr} - x_i + (y_i - y_{nt})\, n \cdot \Delta\theta}{c} \right) \right) \\ &= \exp(j2\pi\eta) \sum_{n=1}^{N} \exp\left(j2\pi \frac{2}{c} \left(f_0 (y_i - y_{nt})\, n \cdot \Delta\theta + f(n)(x_{nr} - x_i) + f(n)(y_i - y_{nt})\, n \cdot \Delta\theta \right) \right) \end{aligned} \tag{10}$$

where $\eta = 2f_0(x_{nr} - x_i)/c$, in general, $f_0 \gg f(n)$, $1 \gg \omega t_n = n \cdot \Delta\theta$. Then the third term $f(n)(y_i - y_{nt})n \cdot \Delta\theta$ of the exponential in the above formula can be ignored. If the frequency increment is $f(n) = n \cdot \Delta f$, Δf is frequency offset. Then, Equation (10) can be regarded as an geometric sequence, so that the two-dimensional imaging result of scattering point (x_i, y_i) can be obtained as follows:

$$\mathbf{S}(nr, nt) = \left| \frac{\sin\left\{ N\pi \left(\frac{2}{c} \left(f_0 \cdot \Delta\theta\, (y_i - y_{nt}) + \Delta f\, (x_{nr} - x_i) \right) \right) \right\}}{\sin\left\{ \pi \left(\frac{2}{c} \left(f_0 \cdot \Delta\theta\, (y_i - y_{nt}) + \Delta f\, (x_{nr} - x_i) \right) \right) \right\}} \right| \tag{11}$$

The above equation is similar to the "sinc" function. Therefore, when $2 \cdot (f_0 \cdot \Delta\theta \cdot \Delta\tilde{y} + \Delta f \cdot \Delta\tilde{x})/c = k$, $k = 0, 1, 2, ...$, the maximum value of coherent accumulation is obtained in Equation (11), where $\Delta\tilde{y} = y_i - y_{nt}$, $\Delta\tilde{x} = x_{nr} - x_i$. When k is a fixed value, $2 \cdot (f_0 \cdot \Delta\theta \cdot \Delta\tilde{y} + \Delta f \cdot \Delta\tilde{x})/c = k$ is a line, that is, the two-dimensional imaging result of the scattered point (x_i, y_i) is a line. However, $k = 0, 1, 2, ...$, so multiple lines may appear in the imaging region. Therefore, linear frequency increment will result in false scattering points and periodicity of imaging results, so that effective imaging results cannot be obtained. The two-dimensional imaging results of a single scattering point located at the center of the imaging scene are shown in Fig. 4.

Figure 4(a) is the imaging result of removing the third exponential item $n \cdot \Delta f_n (y_i - y_{nt}) n \cdot \Delta\theta$ in Equation (10), and Fig. 4(b) is the imaging result containing $n \cdot \Delta f_n (y_i - y_{nt}) n \cdot \Delta\theta$. It can be seen from Fig. 4(a) that the imaging of linear frequency increment signal will cause false scattering points and make the imaging results periodic on the x-axis and y-axis. In the case of removing $n \cdot \Delta f \cdot \Delta\tilde{y} \cdot n \cdot \Delta\theta$,

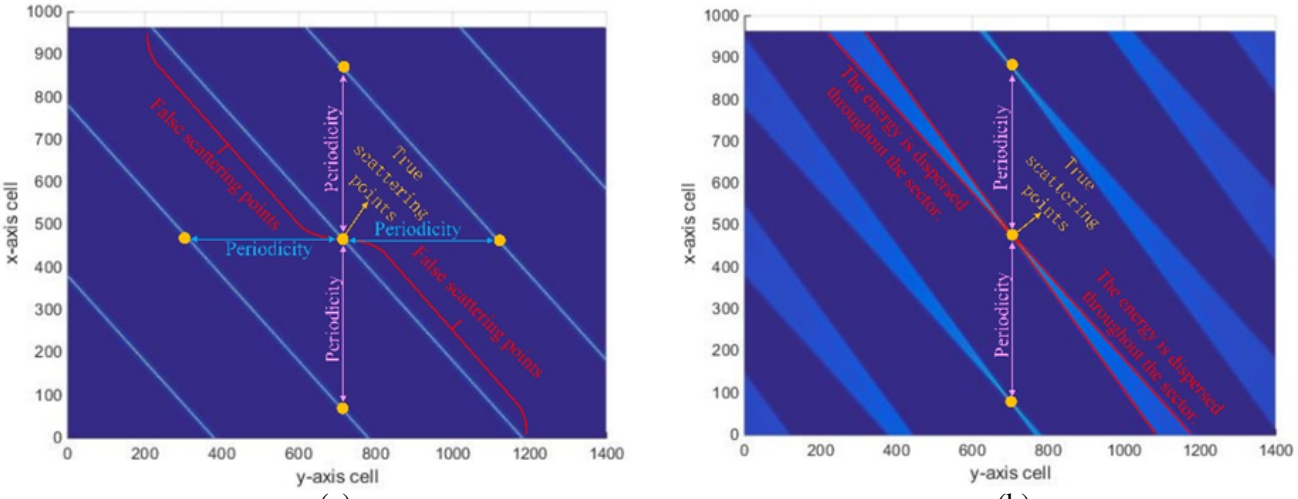

Figure 4. Imaging results of the target with constant frequency increment. (a) Remove the $n \cdot \Delta f \cdot \Delta\tilde{y} \cdot n \cdot \Delta\theta$. (b) Contains the $n \cdot \Delta f \cdot \Delta\tilde{y} \cdot n \cdot \Delta\theta$.

when $\Delta\tilde{y} = 0$, Equation (10) is the sum of a complex exponential signal that constitutes a harmonic relationship, and its fundamental frequency is $2\Delta f/c$. When $\Delta\tilde{x} = 0$, Equation (10) is also the sum of a complex exponential signal that constitutes a harmonic relationship, and its fundamental frequency is $2f_0 \cdot \Delta\theta/c$. Therefore, the periods of Equation (10) on the x-axis and y-axis are:

$$T_x = \frac{c}{2 \cdot \Delta f} \tag{12a}$$

$$T_y = \frac{c}{2f_0 \cdot \Delta\theta} \tag{12b}$$

It can be seen from Fig. 4(b) that compared with Fig. 4(a), the energy on the line is dispersed, greatly reducing the false scattering points. This is because the $n \cdot \Delta f_n(y_i - y_{nt})n \cdot \Delta\theta$ term is related to n, so that in the process of phase-coherent accumulation, the phase-coherent property of data at positions other than the real scattering points on the line will drift. On the other hand, when $\Delta\tilde{x} = 0$, due to the existence of $n \cdot \Delta f_n(y_i - y_{nt})n \cdot \Delta\theta$ term, Equation (10) is no longer the sum of a complex exponential signal that constitutes a harmonic relationship. Therefore, the period of Equation (10) is the minimum value divisible into all complex exponential signal periods $1/\widehat{k}_n$, where $\widehat{k}_n = 2(nf_0 \cdot \Delta\theta + n^2\Delta f \cdot \Delta\theta)/c$. Then the period of Equation (10) on the y-axis can be written as:

$$\widehat{T}_y = \frac{c}{2 \cdot \Delta\theta \langle F_1, F_2, ...F_N \rangle} \tag{13}$$

where $F_n = nf_0 + n^2 \cdot \Delta f$, $\langle \cdot \rangle$ is the operation of taking the greatest common divisor. Because $f_0 \gg N \cdot \Delta f$, $\langle F_1, F_2, ...F_N \rangle \ll f_0$, and then $\widehat{T}_y \gg T_y$. As can be seen from Fig. 4(b), the periodicity of the target image on the y-axis cannot be seen at the same scene size, which, to some extent, expands the no blur imaging range of the radar in the y-axis direction. The periodicity on the x-axis is the same as described earlier.

If $f(n)$ is the increment of random multiplication frequency, $f(n) = h_n \cdot \Delta f$, where h_n is a random positive integer. Therefore, Equation (10) can no longer form a geometric sequence. Only if $\Delta\tilde{y} = 0$, $\Delta\tilde{x} = 0$, the coherent accumulation can be obtained at each observation time, thus obtaining the maximum value of the function, so no false scattering point will be generated. However, this random frequency multiplication increment does not change its periodicity. The period on the x-axis is still Equation (12a), and the period on the y-axis is still Equation (13). From the above analysis, it can be seen that the increment of random multiplication frequency can eliminate the false scattering points and increase the periodicity on the y-axis to some extent. Therefore, it is more reasonable to choose random multiplication frequency increment as the base band signal of FDISAR imaging system.

3.3. Resolution Analysis of Random Multiplication Frequency Increment

In this paper, we introduce the boundary of the half-power resolution in the x-axis direction and y-axis direction, and model and analyze the half-power resolution of the scattering point imaging model (Equation (10)) by referring to the literature [26]. After ignoring the $n \cdot \Delta f_n(y_i - y_{nt})n \cdot \Delta\theta$ term, Equation (10) can be abbreviated as:

$$S_R\left(\Delta\tilde{x}, \Delta\tilde{y}\right) = \exp\left(j2\pi\gamma\right) \sum_{n=1}^{N} \exp\left(j2\pi \frac{2}{c}\left(f_0 \cdot \Delta\tilde{y} \cdot n \cdot \Delta\theta + f\left(n\right) \cdot \Delta\tilde{x}\right)\right) \tag{14}$$

In the case of other parameters being the same, the combination $\mathbf{f} = [f(1), f(2), ...f(N)]$ of frequency increments transmitted at different times affects the boundary of the half-power resolution. Then the half-power resolution boundary can be expressed as:

$$\left|S_R\left(\Delta\tilde{x}_B, \Delta\tilde{y}_B; \mathbf{f}\right)\right|^2 = N^2/2 \tag{15}$$

where $(\Delta\tilde{x}_B, \Delta\tilde{y}_B)$ is the point at which the power of $S_R(\Delta\tilde{x}, \Delta\tilde{y})$ is reduced to half. The general equation that the half-power resolution boundary is an ellipse is derived as:

$$\begin{aligned} \mathbf{S} &= \left|S_R\left(\Delta\tilde{x}_B, \Delta\tilde{y}_B; \mathbf{f}\right)\right|^2 = N^2/2 \\ &= \left|\sum_{n=1}^{N} \exp\left(j2\pi \frac{2}{c}\left(n \cdot f_0 \cdot \Delta\tilde{y}_B \cdot \Delta\theta + \mathbf{f}\left(n\right) \cdot \Delta\tilde{x}_B\right)\right)\right|^2 = \left|\sum_{n=1}^{N} e^{jz_n}\right|^2 \end{aligned} \tag{16}$$

where $z_n = A\mathbf{f}(n) + Bn$, $A = 4\pi \cdot \Delta\tilde{x}_B/c$, $B = 4\pi f_0 \cdot \Delta\theta \cdot \Delta\tilde{y}_B/c$. According to Euler's formula, it can be rewritten as:

$$\left|\sum_{n=1}^{N} e^{jz_n}\right|^2 = \sum_{n=1}^{N} \cos z_n \sum_{m=1}^{N} \cos z_m + \sum_{n=1}^{N} \sin z_n \sum_{m=1}^{N} \sin z_m = \sum_{n=1}^{N} \sum_{m=1}^{N} \cos\left(z_n - z_m\right) \tag{17}$$

By second-order Taylor expansion, Equation (17) can be simplified to:

$$\left|\sum_{n=1}^{N} e^{jz_n}\right|^2 = \sum_{n=1}^{N} \sum_{m=1}^{N} \cos\left(z_n - z_m\right) \approx \sum_{n=1}^{N} \sum_{m=1}^{N} \left[1 - \frac{1}{2}\left(z_n - z_m\right)^2\right] = N^2/2 \tag{18}$$

Equation (18) can be written as:

$$\sum_{n=1}^{N} \sum_{m=1}^{N} \left(z_n - z_m\right)^2 = N^2 \tag{19}$$

Finally, the formula of the half-power resolution described by the general elliptic equation can be achieved as:

$$\begin{aligned} \sum_{n=1}^{N} \sum_{m=1}^{N} \left(z_n - z_m\right)^2 &= \sum_{n=1}^{N} \sum_{m=1}^{N} A^2\left[f\left(n\right) - f\left(m\right)\right]^2 + 2AB\left[f\left(n\right) - f\left(m\right)\right]\left(n - m\right) + B^2\left(n - m\right)^2 \\ &= a\left(\mathbf{f}\right)\left(\Delta\tilde{x}_B\right)^2 + b\left(\mathbf{f}\right) \cdot \Delta\tilde{x}_B \cdot \Delta\tilde{y}_B + C\left(\mathbf{f}\right) \cdot \left(\Delta\tilde{y}_B\right)^2 = N^2 \end{aligned} \tag{20}$$

where $a(\mathbf{f}) = (4\pi/c)^2(\sum_{n=1}^{N}\sum_{m=1}^{N}[f(n) - f(m)]^2)$, $b(\mathbf{f}) = 2(4\pi/c)^2 \cdot f_0 \cdot \Delta\theta \cdot [\sum_{n=1}^{N}\sum_{m=1}^{N}[f(n) - f(m)](n - m)]$, $C(\mathbf{f}) = (4\pi f_0 \cdot \Delta\theta/c)^2[N^2(N^2 - 1)/6]$. The derivation process of the ellipse general form of the above half-power resolution is similar to that in literature [26]. As can be seen from Equation (20), when $a(\mathbf{f})$, $b(\mathbf{f})$ and $C(\mathbf{f})$ are all non-zero elements, the half power resolution is an oblique ellipse. The schematic diagram of the half-power resolution boundary is shown in Fig. 5.

In order to obtain the resolution in the x-axis and y-axis directions, we need to further derive the long axis, short axis, and inclined angle of the oblique ellipse, and the specific process can be described as:

$$a\left(\mathbf{f}\right)\left(\Delta\tilde{x}_B\right)^2 + b\left(\mathbf{f}\right) \cdot \Delta\tilde{x}_B \cdot \Delta\tilde{y}_B + c\left(\mathbf{f}\right) \cdot \left(\Delta\tilde{y}_B\right)^2 - N^2 = 0 \tag{21}$$

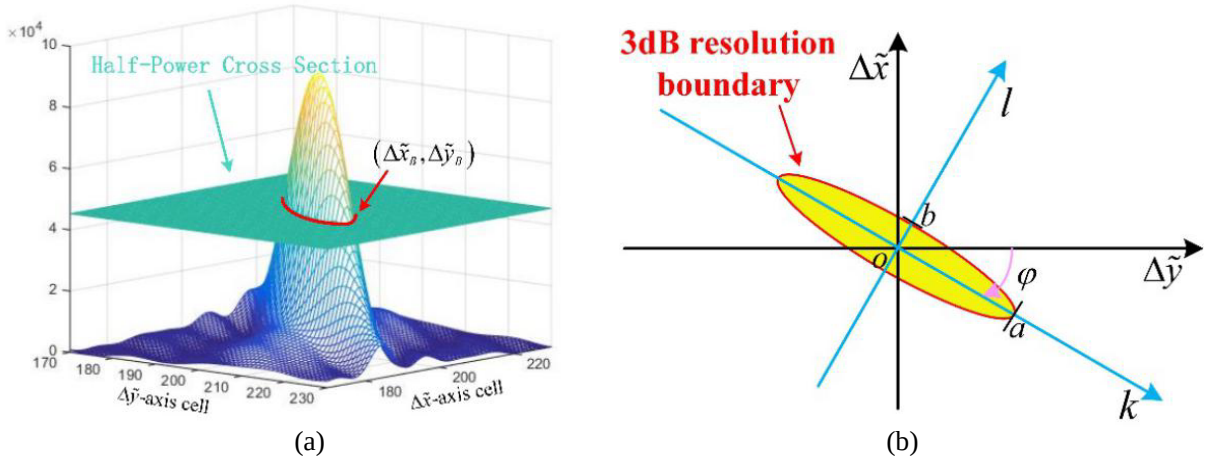

Figure 5. Half power resolution boundary diagram. (a) Half-power resolution boundary 3D schematic diagram. (b) Half-power resolution boundary 2D schematic diagram.

The coordinate transformation formula in Fig. 5(b) can be written as:

$$\begin{bmatrix} \Delta\tilde{y}_B \\ \Delta\tilde{x}_B \end{bmatrix} = \begin{bmatrix} \cos\varphi & -\sin\varphi \\ \sin\varphi & \cos\varphi \end{bmatrix} \begin{bmatrix} k \\ l \end{bmatrix} \tag{22}$$

Substitute Equation (22) into Equation (21), then:

$$\tilde{A}l^2 + \tilde{B}lk + \tilde{C}k^2 + \tilde{F} = 0 \tag{23}$$

where $\tilde{A} = a(\mathbf{f})\cos^2\varphi - b(\mathbf{f})\sin\varphi\cos\varphi + c(\mathbf{f})\sin^2\varphi$, $\tilde{B} = 2(a(\mathbf{f}) - c(\mathbf{f}))\sin\varphi\cos\varphi + b(\mathbf{f})(\cos^2\varphi - \sin^2\varphi)$, $\tilde{C} = a(\mathbf{f})\sin^2\varphi + b(\mathbf{f})\sin\varphi\cos\varphi + c(\mathbf{f})\cos^2\varphi$, $\tilde{F} = -N^2$. After the coordinate transformation, the inclined angle of the oblique ellipse equation under the kol coordinate axis will be zero, that is $\tilde{B} = 0$, then:

$$\tilde{B} = 2\left(c\left(\mathbf{f}\right) - a\left(\mathbf{f}\right)\right)\sin\varphi\cos\varphi + b\left(\mathbf{f}\right)\left(\cos^2\varphi - \sin^2\varphi\right) = 0 \tag{24}$$

Equation (24) is simplified as:

$$\cot\left(2\varphi\right) = \frac{a\left(\mathbf{f}\right) - c\left(\mathbf{f}\right)}{b\left(\mathbf{f}\right)} \tag{25}$$

Then the inclined angle can be expressed as:

$$\varphi = \begin{cases} 0 & \text{for } b\left(\mathbf{f}\right) = 0 \text{ and } a\left(\mathbf{f}\right) < c\left(\mathbf{f}\right) \\ \dfrac{1}{2}\pi & \text{for } b\left(\mathbf{f}\right) = 0 \text{ and } a\left(\mathbf{f}\right) > c\left(\mathbf{f}\right) \\ \dfrac{1}{2}\cot^{-1}\left(\dfrac{a\left(\mathbf{f}\right) - c\left(\mathbf{f}\right)}{b\left(\mathbf{f}\right)}\right) & \text{for } b\left(\mathbf{f}\right) \neq 0 \text{ and } a\left(\mathbf{f}\right) < c\left(\mathbf{f}\right) \\ \dfrac{\pi}{2} + \dfrac{1}{2}\cot^{-1}\left(\dfrac{a\left(\mathbf{f}\right) - c\left(\mathbf{f}\right)}{b\left(\mathbf{f}\right)}\right) & \text{for } b\left(\mathbf{f}\right) \neq 0 \text{ and } a\left(\mathbf{f}\right) > c\left(\mathbf{f}\right) \end{cases} \tag{26}$$

Equation (23) can be further written as:

$$\tilde{A}l^2 + \tilde{C}k^2 + \tilde{F} = 0 \tag{27}$$

Then the square of the semi-long axis and the semi-short axis of the ellipse can be written as:

$$a^2 = \frac{-2N^2}{\sqrt{\left[a\left(\mathbf{f}\right) - c\left(\mathbf{f}\right)\right]^2 + b^2\left(\mathbf{f}\right)} - \left[a\left(\mathbf{f}\right) + c\left(\mathbf{f}\right)\right]} \tag{28a}$$

$$b^2 = \frac{-2N^2}{-\sqrt{\left[a\left(\mathbf{f}\right) - c\left(\mathbf{f}\right)\right]^2 + b^2\left(\mathbf{f}\right)} - \left[a\left(\mathbf{f}\right) + c\left(\mathbf{f}\right)\right]} \tag{28b}$$

We choose twice the maximum projection value of the half power resolution boundary on the $\Delta\tilde{x}$-axis as the resolution in the x-axis direction, and choose twice the maximum projection value on the $\Delta\tilde{y}$-axis as the resolution in the y-axis direction. Then the resolutions in the x-axis direction and y-axis direction can be described as:

$$\rho_x = 2 \cdot \max\left(\sqrt{a^2}\left|\sin\varphi\right|, \sqrt{b^2}\left|\cos\varphi\right|\right) \tag{29a}$$

$$\rho_y = 2 \cdot \max\left(\sqrt{a^2}\left|\cos\varphi\right|, \sqrt{b^2}\left|\sin\varphi\right|\right) \tag{29b}$$

3.4. BP Hybrid Imaging Algorithm Based on Compressed Sensing

When the radar transmits the increment of random multiplication frequency signal, the energy on the straight line in Fig. 4(a) except the real target point will be distributed randomly in the entire imaging area. In the case of a certain number of emitted pulses, the energy intensity of this random distribution will increase with the increase of the number of scattering points of the target, which will eventually affect the image quality. In order to improve the image quality, a BP hybrid algorithm based on compressed sensing is proposed based on the theory of compressed sensing. The compression perception theory shows that as long as the signal in a transform domain is sparse or compressible, an observation matrix that is not coherent with the sparse transform matrix can be used to project high-dimensional signals into a low-dimensional space. Finally, by solving an optimization problem, the original signal can be reconstructed from a small amount of projection information with high probability [27, 28]. During the imaging process, the energy of the target echo signal is only determined by a few scattering centers [29], which makes it possible to realize the BP hybrid imaging algorithm based on compressed sensing.

From the above analysis, it can be seen that the echo signal with the increment of random multiplication frequency is periodic. Therefore, in order to achieve blur-free imaging range imaging, the frequency offset of the transmitted signal should meet the following requirements:

$$\Delta\bar{f} \leq \frac{c}{2 \cdot L_{\max}} \tag{30}$$

where $L_{\max}$ is the maximum blur-free imaging distance in the X-axis direction. The echo after mixing is written in the form of a vector $\mathbf{S}_r = [s_r(t_1), s_r(t_2), ...s_r(t_N)]$. The frequency increment of the transmitted signal at time t_n is $f_n = h_n \cdot \Delta\bar{f}$, where h_n is a random positive integer between 1 and N. The data processing diagram of the improved BP imaging algorithm is shown in Fig. 6.

Finding a sparse transformation matrix makes the projection of the echo signal sequence $\mathbf{S}_r$ on it sparse, which is one of the keys of the imaging algorithm based on compressed sensing. The result of the improved BP imaging algorithm is sparse. Therefore, it is essential to write "Data processing" in Fig. 6

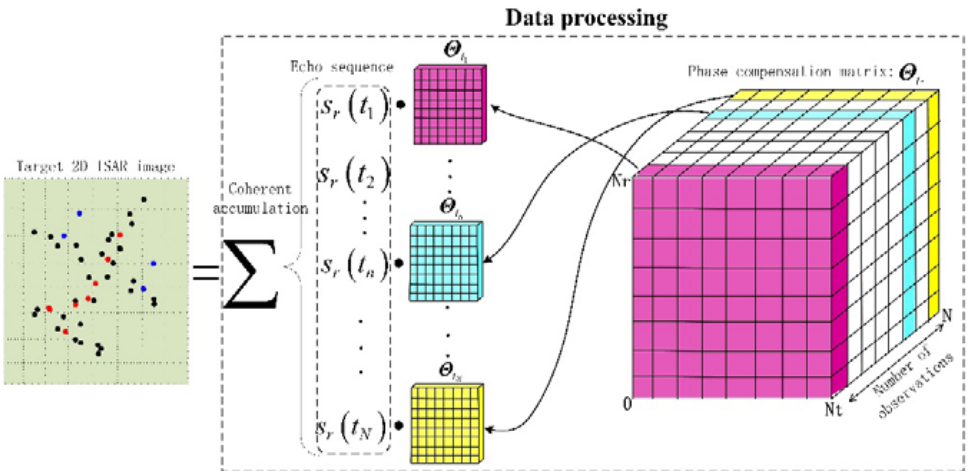

Figure 6. Schematic diagram of data processing for improved BP imaging algorithm.

in the form of matrix multiplication to find the sparse transformation basis. According to Equation (6), the two-dimensional image of the target can be written as:

$$\mathbf{S} = \left| \sum_{n=1}^{N} \left[s_r\left(t_n\right) \cdot \mathbf{\Theta}_{t_n} \right] \right| \tag{31}$$

We straighten the two-dimensional image matrix and phase compensation matrix, then Equation (31) can be rewritten as:

$$\boldsymbol{\gamma}_{\tilde{N}\times 1} = \mathbf{\Psi}_{\tilde{N}\times N} \cdot \mathbf{S}_r \tag{32}$$

where $\boldsymbol{\gamma}_{\tilde{N}\times 1} = \mathbf{S}\left(:\right)$, $\tilde{N} = N_r \cdot N_t$, $\mathbf{\Psi}_{\tilde{N}\times N}\left(:,n\right) = \mathbf{\Theta}_{t_n}\left(:\right)$, $\left(\mathbf{\Psi}_{\tilde{N}\times N}\right)^H \cdot \mathbf{\Psi}_{\tilde{N}\times N} \approx \mathbf{E}_{N\times N}$, $\left(\cdot\right)^H$ represents the conjugate transpose, and $\mathbf{E}_{N\times N}$ is a single matrix, the specific derivation process as:

$$\left[\mathbf{\Theta}_{t_1}\left(:\right), \mathbf{\Theta}_{t_2}\left(:\right), ...\mathbf{\Theta}_{t_N}\left(:\right)\right]^H \left[\mathbf{\Theta}_{t_1}\left(:\right), \mathbf{\Theta}_{t_2}\left(:\right), ...\mathbf{\Theta}_{t_N}\left(:\right)\right] = \bar{\mathbf{E}} \tag{33}$$

Then the element of matrix $\bar{\mathbf{E}}$ at position (n,k) can be written as:

$$\bar{\mathbf{E}}\left(n,k\right) = \left[\mathbf{\Theta}_{t_n}\left(:\right)\right]^H \mathbf{\Theta}_{t_k}\left(:\right) = \sum\sum e^{-j2\pi f_n \frac{2R_{nr,nt}(t_n)}{c}} e^{j2\pi f_k \frac{2R_{kr,kt}(t_k)}{c}} \tag{34}$$

Substitute Equation (9) into Equation (34) as:

$$\bar{\mathbf{E}}\left(n,k\right) = \sum\sum e^{-j2\pi f_n \frac{2(R_0+x_{nr}-y_{nt}\cdot n\cdot\Delta\theta+V_r t_n)}{c}} e^{j2\pi f_k \frac{2(R_0+x_{kr}-y_{kt}\cdot k\cdot\Delta\theta+V_r t_k)}{c}} \tag{35}$$

Since formula (35) is the sum of the multiplication of the corresponding elements of the conjugate transpose of the phase compensation matrix at the time of t_n and the phase compensation matrix at the time of t_k, more specifically, it is the inner product of the phase compensation term at the grid point corresponding to the time of t_n and time of t_k. Therefore, there is $x_{nr} = x_{kr}$, $y_{nr} = y_{kr}$ in the above equation, so Equation (35) can be abbreviated as:

$$\begin{aligned}
\bar{\mathbf{E}}\left(n,k\right) &= \sum_{nr=1}^{N_r}\sum_{nt=1}^{N_t} e^{j2\pi \frac{2f_k\left(R_0+x_{nr}-y_{nt}\cdot k\cdot\Delta\theta+V_r t_k\right)-2f_n(R_0+x_{nr}-y_{nt}\cdot n\cdot\Delta\theta+V_r t_n)}{c}} \\
&= \sum_{nr=1}^{N_r}\sum_{nt=1}^{N_t} e^{j2\pi \frac{2f_k(x_{nr}-y_{nt}\cdot k\cdot\Delta\theta)-2f_n(x_{nr}-y_{nt}\cdot n\cdot\Delta\theta)}{c}} e^{j2\pi \frac{2f_k\left(R_0+V_r t_k\right)-2f_n(R_0+V_r t_n)}{c}} \\
&= \beta \sum_{nr=1}^{N_r}\sum_{nt=1}^{N_t} e^{j4\pi \frac{(f_k-f_n)x_{nr}+(f_n\cdot n\cdot\Delta\theta-f_k\cdot k\cdot\Delta\theta)y_{nt}}{c}} \\
&= \beta \sum_{nr=1}^{N_r}\sum_{nt=1}^{N_t} e^{j\frac{4\pi(f_k-f_n)}{c}x_{nr}} e^{j\frac{4\pi(f_n\cdot n\cdot\Delta\theta-f_k\cdot k\cdot\Delta\theta)}{c}y_{nt}}
\end{aligned} \tag{36}$$

where $\beta = e^{j2\pi \frac{2f_k(R_0+V_r t_k)-2f_n(R_0+V_r t_n)}{c}}$ is constant term. Because of $x_{nr} = -(N_r/2)\cdot\Delta x + nr\cdot\Delta x$, $y_{nt} = -(N_t/2)\cdot\Delta y + nt\cdot\Delta y$, Equation (45) can be written as:

$$\begin{aligned}
\bar{\mathbf{E}}\left(n,k\right) &= \beta \sum_{nr=-N_r/2}^{N_r/2}\sum_{nt=-N_t/2}^{N_r/2} e^{j\frac{4\pi(f_k-f_n)\cdot\Delta x}{c}nr} e^{j\frac{4\pi(f_n\cdot n\cdot\Delta\theta-f_k\cdot k\cdot\Delta\theta)\cdot\Delta y}{c}nt} \\
&= \beta \sum_{nr=-N_r/2}^{N_r/2} e^{j\frac{4\pi(f_k-f_n)\cdot\Delta x}{c}nr} \sum_{nt=-N_t/2}^{N_r/2} e^{j\frac{4\pi(f_n\cdot n\cdot\Delta\theta-f_k\cdot k\cdot\Delta\theta)\cdot\Delta y}{c}nt} \\
&= \beta \sum_{nr=-N_r/2}^{N_r/2} e^{j2\pi\mu\cdot nr} \sum_{nt=-N_t/2}^{N_r/2} e^{j2\pi\nu\cdot nt}
\end{aligned} \tag{37}$$

where $\mu = \frac{2(f_k - f_n)\cdot\Delta x}{c}$ and $\nu = \frac{2(f_n\cdot n\cdot\Delta\theta - f_k\cdot k\cdot\Delta\theta)\cdot\Delta y}{c}$ is constant. Equation (37) is the product of the respective sums of two proportional sequences, which can be further simplified to:

$$\left|\bar{\mathbf{E}}\left(n,k\right)\right| = \left|\sum_{nr=-N_r/2}^{N_r/2} e^{j2\pi\mu\cdot nr} \sum_{nt=-N_t/2}^{N_t/2} e^{j2\pi\nu\cdot nt}\right| = \left|\frac{\sin\left(\pi N_r\mu\right)}{\sin\left(\pi\mu\right)}\right| \cdot \left|\frac{\sin\left(\pi N_t\nu\right)}{\sin\left(\pi\nu\right)}\right| \tag{38}$$

The zero position of the $|\sin(\pi N_r\mu)\sin(\pi\mu)|$ term in Equation (47) is as:

$$N_r\mu = \frac{2\left(f_k - f_n\right)\cdot\Delta x\cdot N_r}{c} = \pm D \tag{39}$$

where D is any positive integer. That is:

$$|f_k - f_n| = D\frac{c}{2\Delta x\cdot N_r} \tag{40}$$

Therefore, we assume that the selected Δf is satisfied as:

$$\Delta f = D\frac{c}{2\Delta x\cdot N_r} \tag{41}$$

This will ensure that in the case of $k \neq n$, $|\bar{\mathbf{E}}(n,k)|$ is close to zero. There are:

$$\left|\bar{\mathbf{E}}\left(n,k\right)\right| = \begin{cases} \tilde{N} & \text{for } k = n \\ \sigma, \sigma \ll \tilde{N} & \text{for } k \neq n \end{cases} \tag{42}$$

So there is $\frac{1}{\tilde{N}}|\bar{\mathbf{E}}| \approx \mathbf{E}$, where $\mathbf{E}$ is the identity matrix. Then Equation (32) can be written as:

$$\mathbf{S}_r = \frac{1}{\tilde{N}}\left(\boldsymbol{\Psi}_{\tilde{N}\times N}\right)^H \gamma_{\tilde{N}\times 1} \tag{43}$$

It can be seen from Equation (43) that the echo signal $\mathbf{S}_r$ can be sparsely represented by $(\boldsymbol{\Psi}_{\tilde{N}\times N})^H/\tilde{N}$. Therefore, let $(\boldsymbol{\Psi}_{\tilde{N}\times N})^H/\tilde{N}$ be a sparse transformation matrix and be written as: $\tilde{\boldsymbol{\Psi}}_{\tilde{N}\times N} = (\boldsymbol{\Psi}_{\tilde{N}\times N})^H/\tilde{N}$. In addition, we designed an $M\times N$ observation matrix $\boldsymbol{\Psi}_{M\times N}$ as:

$$\phi\left(m,n\right) = \begin{cases} 1, & \left\{(m,n)\,|\mathbf{sqe}\left(m\right) = n\right\} \\ 0, & \text{else} \end{cases} \tag{44}$$

where $M \geq c_1 K\ln(N)$; K is the number of non-zero elements in $\boldsymbol{\gamma}_{\tilde{N}\times 1}$; c_1 is a constant between 0.5 and 2; **sqe** is a sequence composed of M numbers randomly selected from the set $[1, N]$ without repeating. It can be easily proved that $\boldsymbol{\Phi}_{M\times N}$ and $\tilde{\boldsymbol{\Psi}}_{N\times\tilde{N}}$ are incoherent [30]. Therefore, the target two-dimensional image $\boldsymbol{\gamma}_{\tilde{N}\times 1}$ can be reconstructed by optimizing the following formula:

$$\begin{aligned} \boldsymbol{\gamma} &= \min\left\|\boldsymbol{\gamma}\right\|_1, \\ s.t.\ \mathbf{Y} &= \boldsymbol{\Phi}_{M\times N}\tilde{\boldsymbol{\Psi}}_{N\times\tilde{N}}\boldsymbol{\gamma}_{\tilde{N}\times 1} \end{aligned} \tag{45}$$

where $\mathbf{Y} = \boldsymbol{\Phi}_{M\times N}\mathbf{S}_r$. Since $\boldsymbol{\Phi}_{M\times N}$ and $\tilde{\boldsymbol{\Psi}}_{N\times\tilde{N}}$ are incoherent, so satisfying the RIP condition, a good optimization result can be obtained through the orthogonal matching pursuit algorithm (OMP) [31].

4. EXPERIMENTAL RESULT

In order to verify the effectiveness of the frequency diverse ISAR two-dimensional imaging method, we perform experiments with simulated and raw data.

4.1. Experiments Using the Simulated Signal

Suppose that the target is located in the center of the scene, and the target is observed for 401 times at the same time interval of the radar. The initial frequency of the radar transmission signal is $f_0 = 10\,\text{GHz}$; the frequency offset is $\Delta f = 1.5\,\text{MHz}$; and the frequency increment is in the form of random frequency multiplication: $f(n) = \tilde{\mathbf{f}}(n)$ is the increment of random multiplication frequency, where $\tilde{\mathbf{f}} = \text{Rand}([0, \Delta f, 2 \cdot \Delta f, ...400\Delta f])$, $\text{Rand}(\cdot)$ represent the positions of randomly scrambled sequence elements. During the imaging process, the angle of the target relative to the radar is 10°, and the distance between the radar and the center of the target is $R_0 = 6\,\text{km}$. The imaging area is divided into grids with a size of 100×100; the grid spacing in the y-axis direction is ρ_y; the grid spacing in the x-axis direction is ρ_x; the grid center is $(50, 50)$. Now set the five scattering points in $(50, 50), (50, 30), (50, 70), (30, 50), (70, 50)$, assuming that the target scattering coefficient is 1. The target imaging effect is shown in Fig. 7.

According to Equation (29), the spacing between adjacent cells in the x-axis direction in Fig. 7 is 0.194 m, and the spacing between adjacent cells in the y-axis direction is 0.067 m. The imaging results of the increment of random multiplication frequency are shown in Fig. 7(b), from which it can be seen

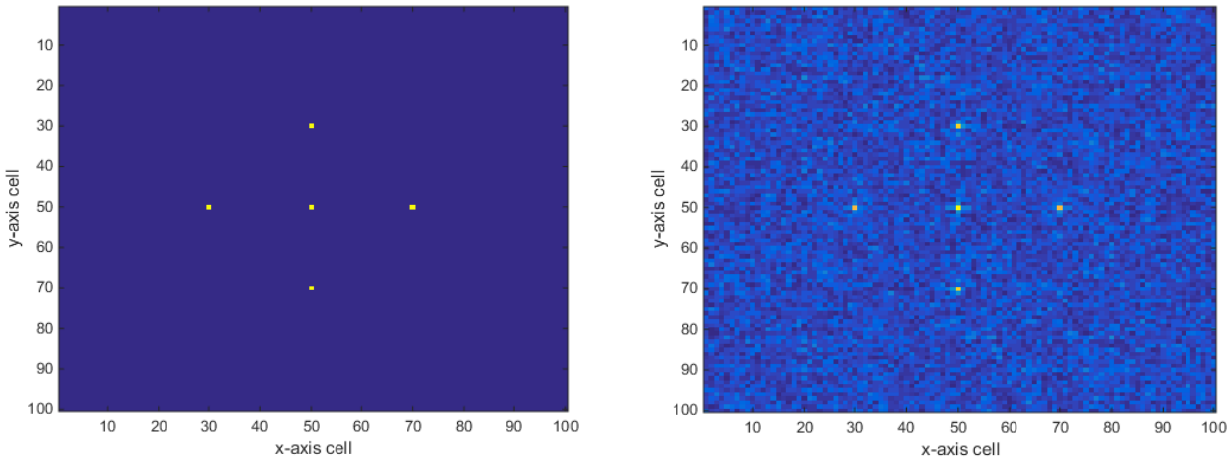

(a) (b)

Figure 7. Comparison of target imaging effects. (a) Multi-scattering target scene graph. (b) Target imaging results the increment of random multiplication frequency.

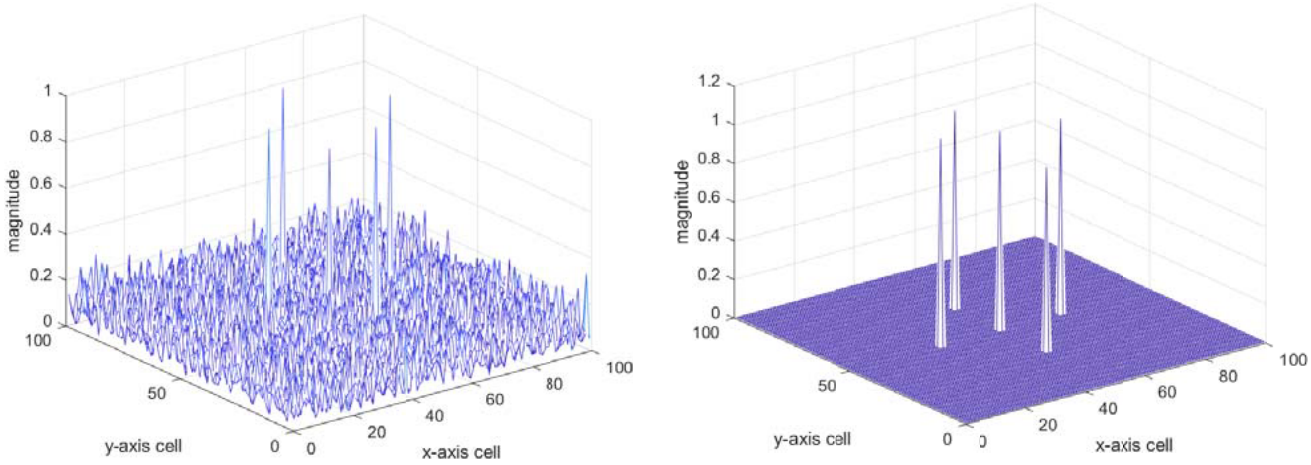

(a) (b)

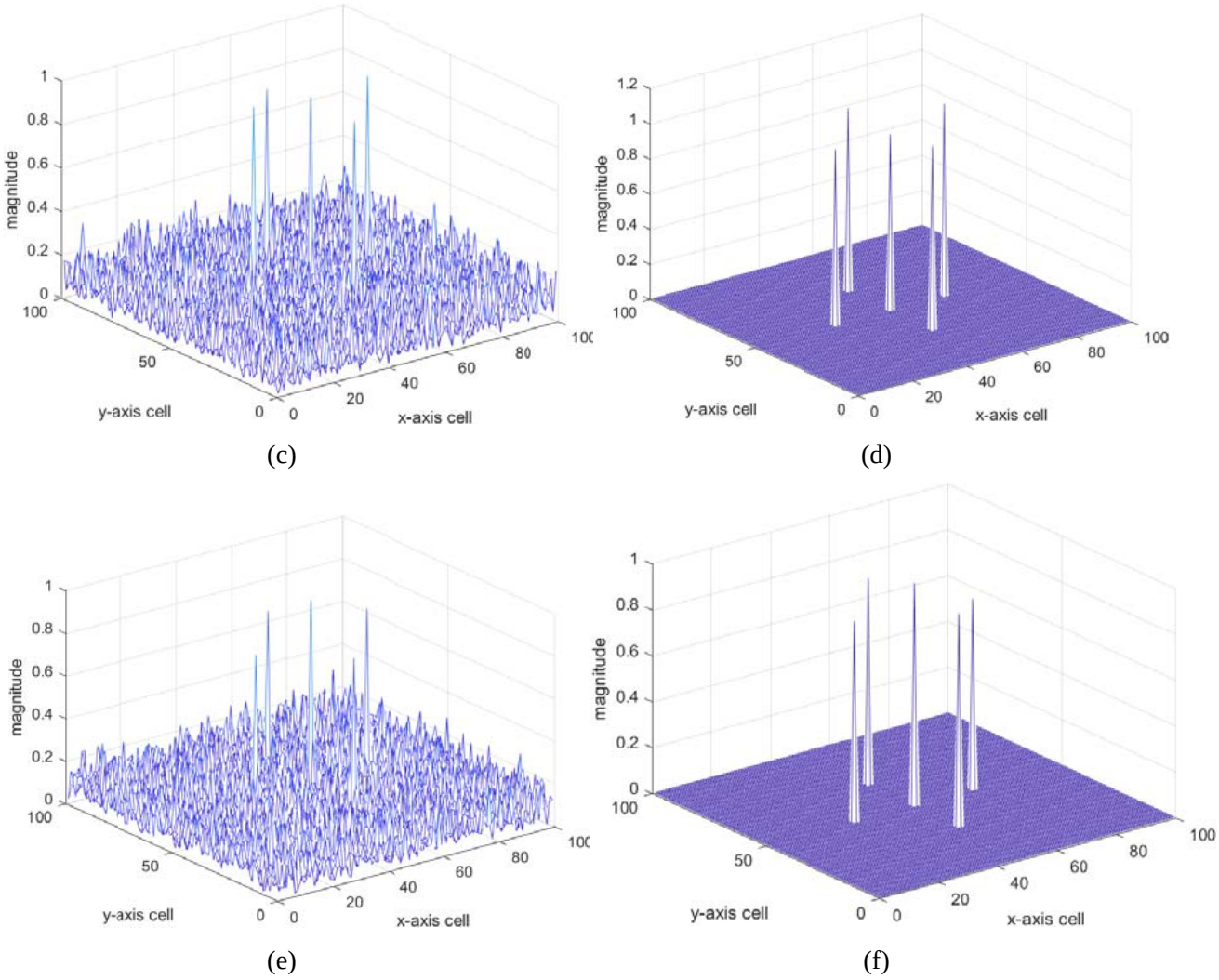

Figure 8. Comparison of three-dimensional imaging results. (a) In the case of a signal-to-noise ratio of 15 dB, three-dimensional imaging results of the increment of random multiplication frequency. (b) In the case of a signal-to-noise ratio of 15 dB, three-dimensional imaging results of BP hybrid imaging based on compressed sensing. (c) In the case of a signal-to-noise ratio of 10 dB, three-dimensional imaging results of the increment of random multiplication frequency. (d) In the case of a signal-to-noise ratio of 10 dB, three-dimensional imaging results of BP hybrid imaging based on compressed sensing. (e) In the case of a signal-to-noise ratio of 5 dB, three-dimensional imaging results of the increment of random multiplication frequency. (f) In the case of a signal-to-noise ratio of 5 dB, three-dimensional imaging results of BP hybrid imaging based on compressed sensing.

that the real relative position of the target is obtained, and there is no false scattering point. From the above imaging simulation results, it can be seen that the improved BP imaging algorithm based on FDISAR proposed in this paper can complete two-dimensional imaging of multi-scattering moving targets. However, it can be seen from Fig. 8(a) that although the increment of random multiplication frequency eliminates the false scattering points and obtains the real relative position of the target, it also generates some side lobe. This phenomenon will be more serious with the increase of scattering points when the number of transmitting pulses is certain. For this reason, we propose a BP hybrid imaging algorithm based on compressed sensing. The imaging results are shown in Fig. 8(b), from which we can see that the algorithm can well reconstruct the two-dimensional image of the target, reduce the influence of the side lobe, and improve the imaging quality.

4.2. Experiments Using the Measured Data

In order to further verify the proposed system and imaging algorithm, we used a single-transmission and single-reception radar to implement imaging experiments. The transceiver antenna is 1.6 m away from the target center. During the imaging process, the angle of the target relative to the radar is 10°. The radar transmits 101 pulse signals to the target at equal intervals. The starting frequency of the radar transmission signal is $f_0 = 10\,\text{GHz}$; the frequency offset is $\Delta f = 20\,\text{MHz}$; the frequency increment $f(n)$ is frequency values randomly selected from the set $[0, \Delta f, 2\Delta f, ...24\Delta f]$. The target optical diagram and the schematic diagram of the experimental system are shown in Fig. 9.

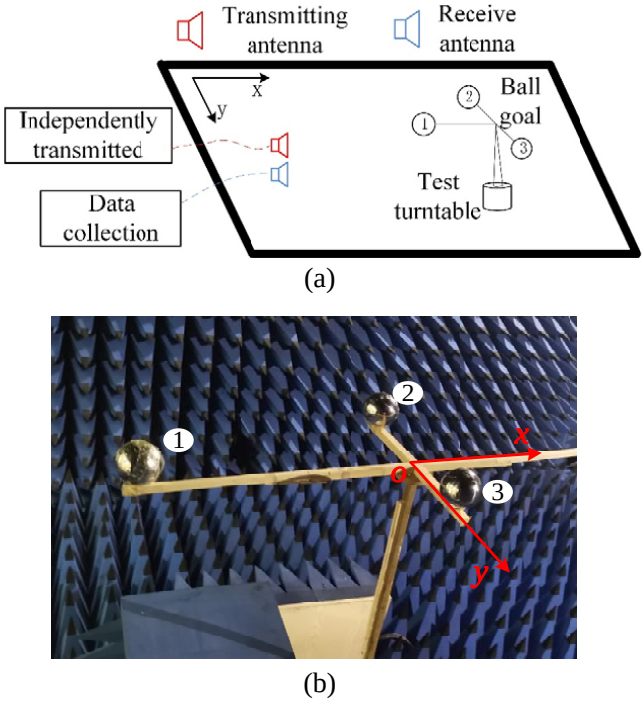

Figure 9. Schematic diagram of target optical photo and test system. (a) Schematic diagram of the test system. (b) Optical photo of target.

The target consists of three metal balls, and the target can rotate around the vertical axis. Taking the intersection point of the connection line of the three balls in Fig. 9(a) as the origin of the coordinate axis, the three balls are placed at the positions of: ball 1 $(-0.50, 0)$, ball 2 $(0, -0.20)$, and ball 3 $(0.13, 0)$, respectively. Calculate the resolutions in the x-axis direction and y-axis direction as 0.2406 m, 0.0663 m respectively by Equation (29), and divide the cells according to the resolution. Using the proposed imaging algorithm, the imaging results of the target are shown in Fig. 10.

It can be seen from Fig. 10(b) that the position of the origin of the coordinate axis is $(11, 11)$. The first ball on the left is ball 1, which is two cells away from the origin of the coordinate, that is, a distance of 0.4812 m. The first ball at the top is 3 cells from ball 2 and the origin of the coordinate, that is, 0.1989 m apart. The first ball at the bottom is the distance between ball 3 and the origin of the coordinates, that is, 0.1326 m. This is basically consistent with the position where the three balls are placed, which further verifies that the FDISAR improved BP imaging algorithm proposed in this paper can achieve blur-free imaging of moving scattering point targets, but it can be seen from Fig. 9 that there are certain side lobes. We have further verified the effectiveness of the BP hybrid algorithm based on compressed sensing. We randomly selected 70 values from the echo data $\mathbf{S}_r$ according to the observation matrix of Equation (44). The reconstruction results obtained are shown in Fig. 11.

Compared with Fig. 10, Fig. 11 obtained a clearer two-dimensional image of the target, reduced the side lobe, and correctly reconstructed the relative position of the target, which verified the effectiveness of the algorithm.

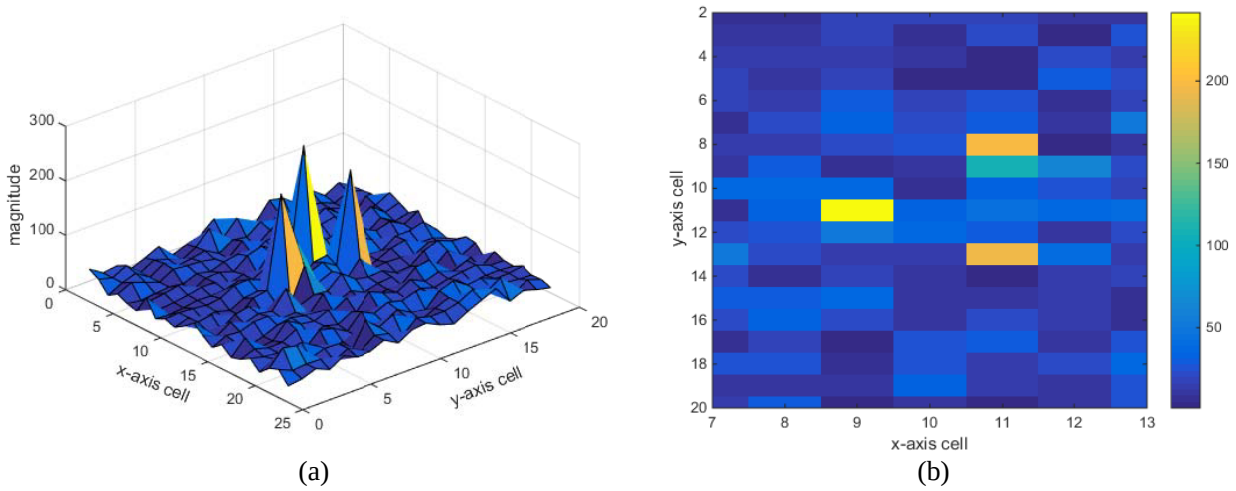

Figure 10. Measured imaging results. (a) 3D image of target imaging result. (b) 2D image of target imaging result.

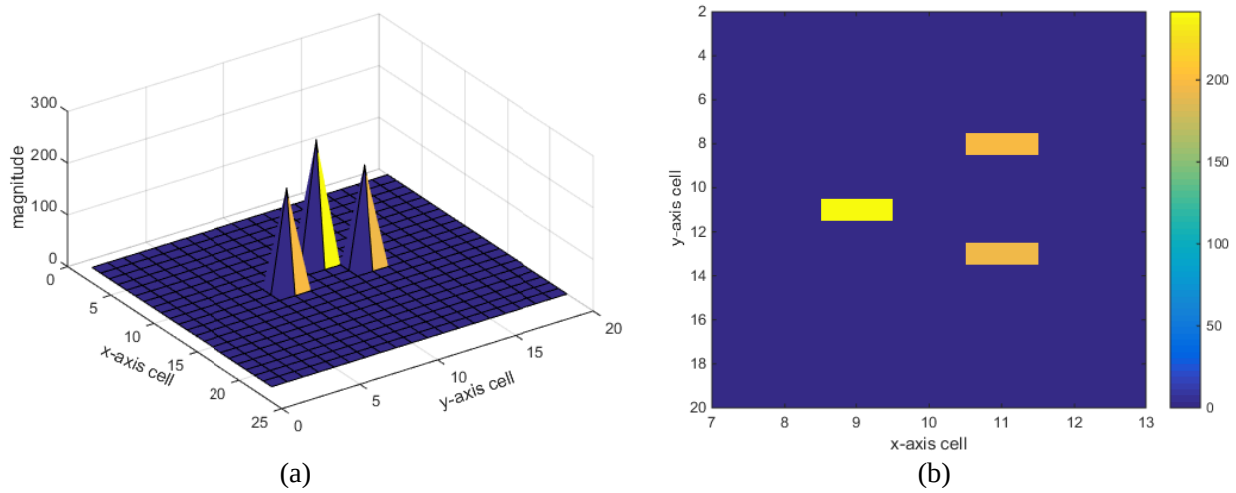

Figure 11. CS-measured imaging results. (a) Three-dimensional display of CS-target imaging results. (b) Two-dimensional display of CS-target imaging results.

5. CONCLUSION

In this paper, an improved BP imaging algorithm based on frequency diversity ISAR is proposed, which combines the idea of frequency diversity and inverse synthetic aperture. The method can transmit signals of different frequencies to the target at different times to synthesize broadband signals and generate synthetic aperture through the relative motion between the target and the radar, finally obtaining the two-dimensional imaging capability of the target. On this basis, the analysis shows that a constant frequency increment will result in the generation of false scattering points, and the increment of random multiplication frequency can eliminate the effect of false points and obtain a two-dimensional imaging result without blurring the target. However, the increment of random multiplication frequency causes the energy other than the real target point to be randomly dispersed in the entire imaging area, causing a certain degree of side lobe rise in the imaging result, which affects the imaging quality. In response to this situation, we combined the improved BP imaging algorithm with the theory of compressed sensing

to propose a BP hybrid imaging algorithm based on compressed sensing, and finally obtained a high-quality target 2D image, reducing the impact of imaging side lobes and improving imaging quality. In the simulation and actual measurement experiments, the effectiveness of the imaging method of the FDISAR imaging system proposed in this paper is verified. Because FDISAR does not need to transmit broadband signals, and the bandwidth can be flexibly adjusted during the imaging process, the application of this method is of great significance for reducing the complexity and cost of the ISAR imaging system and improving the flexibility of the system's control bandwidth resources.

ACKNOWLEDGMENT

This work was supported by the National Natural Science Foundation of China (61871425), National Natural Science Foundation of Guangxi (2021GXNSFAA220051), Guangxi Key Laboratory of Wireless Wideband Communication and Signal Processing References.

REFERENCES

1. Zuo, L. and B. Wang, "ISAR imaging of non-uniform rotating targets based on optimized matching fourier transform," *IEEE Access*, Vol. 8, 64324–64330, 2020.
2. Kang, B. S., K. Lee, and K. T. Kim, "Image registration for 3-D interferometric-ISAR imaging through joint-channel phase difference functions," *IEEE Transactions on Aerospace and Electronic Systems*, Vol. 57, No. 1, 22–38, 2021.
3. Hu, C., L. Wang, Z. Li, and D. Zhu, "Inverse synthetic aperture radar imaging using a fully convolutional neural network," *IEEE Geoscience and Remote Sensing Letters*, Vol. 17, No. 7, 1203–1207, 2020.
4. Cheng, P., J. Cheng, X. Wang, and J. Zhao, "An ISAR imaging method based on improved CAMP algorithm," *IEEE Sensors Journal*, Vol. 21, No. 12, 13514–13521, 2021.
5. Stankovic, L., "ISAR image analysis and recovery with unavailable or heavily corrupted data," *IEEE Transactions on Aerospace and Electronic Systems*, Vol. 51, No. 3, 2093–2106, 2015.
6. Ji, B., Y. Wang, B. Zhao, X. Lu, and R. Xu, "Novel super-resolution ISAR imaging method via two-dimensional unitary matrix pencil algorithm," *2020 15th IEEE International Conference on Signal Processing (ICSP)*, Vol. 1, 600–604, 2020.
7. Zhang, S., Y. Liu, and X. Li, "Bayesian bistatic ISAR imaging for targets with complex motion under low SNR condition," *IEEE Transactions on Image Processing*, Vol. 27, No. 5, 2447–2460, 2018.
8. Zhang, S., Y. Liu, X. Li, and G. Bi, "Fast ISAR cross-range scaling using modified newton method," *IEEE Transactions on Aerospace and Electronic Systems*, Vol. 54, No. 3, 1355–1367, 2018.
9. Hu, J., J. Zhang, Q. Zhai, R. Zhan, and D. Lu, "ISAR imaging using a new stepped-frequency signal format," *IEEE Transactions on Geoscience and Remote Sensing*, Vol. 52, No. 7, 4291–4305, 2014.
10. Zhang, L., Z. Qiao, M. Xing, Y. Li, and Z. Bao, "High-resolution ISAR imaging with sparse stepped-frequency waveforms," *IEEE Transactions on Geoscience and Remote Sensing*, Vol. 49, No. 11, 4630–4651, 2011.
11. Yeh, C. M., et al., "Rotational motion estimation for ISAR via triangle pose difference on two range-Doppler images," *IET Radar Sonar & Navigation*, Vol. 4, No. 4, 528–536, 2010.
12. Berizzi, F., E. D. Mese, M. Diani, and M. Martorella, "High-resolution ISAR imaging of maneuvering targets by means of the range instantaneous Doppler technique: Modeling and performance analysis," *IEEE Transactions on Image Processing*, Vol. 10, No. 12, 1880–1890, 2001.
13. Munoz-Ferreras, J. M. and F. Perez-Martinez, "On the Doppler spreading effect for the range-instantaneous-doppler technique in inverse synthetic aperture radar imagery," *IEEE Geoscience and Remote Sensing Letters*, Vol. 7, No. 1, 180–184, 2010.

14. Wang, Y. and Y. Lin, "ISAR imaging of non-uniformly rotating target via range-instantaneous-Doppler-derivatives algorithm," *IEEE Journal of Selected Topics in Applied Earth Observations and Remote Sensing*, Vol. 7, No. 1, 167–176, 2014.
15. Liu, Q., A. Liu, Y. Wang, and H. Li, "A super-resolution sparse aperture ISAR sensors imaging algorithm via the MUSIC technique," *IEEE Transactions on Geoscience and Remote Sensing*, Vol. 57, No. 9, 7119–7134, 2019.
16. Zhang, S., et al., "High-resolution bistatic ISAR imaging based on two-dimensional compressed sensing," *IEEE Transactions on Antennas and Propagation*, Vol. 63, No. 5, 2098–2111, 2015.
17. Jiu, B., H. Liu, H. Liu, L. Zhang, Y. Cong, and Z. Bao, "Joint ISAR imaging and cross-range scaling method based on compressive sensing with adaptive dictionary," *IEEE Transactions on Antennas and Propagation*, Vol. 63, No. 5, 2112–2121, 2015.
18. Rodenbeck, C. T., et al., "Ultra-wideband low-cost phased-array radars," *IEEE Transactions on Microwave Theory and Techniques*, Vol. 53, No. 12, 3697–3703, 2005.
19. Zhang, L., Z. Qiao, M. Xing, J. Sheng, R. Guo, and Z. Bao, "High-resolution ISAR imaging by exploiting sparse apertures," *IEEE Transactions on Antennas and Propagation*, Vol. 60, No. 2, 997–1008, 2012.
20. Zheng, J., T. Su, W. Zhu, L. Zhang, Z. Liu, and Q. H. Liu, "ISAR imaging of nonuniformly rotating target based on a fast parameter estimation algorithm of cubic phase signal," *IEEE Transactions on Geoscience and Remote Sensing*, Vol. 53, No. 9, 4727–4740, 2015.
21. Kang, M., S. Lee, S. Lee, and K. Kim, "ISAR imaging of high-speed maneuvering target using gapped stepped-frequency waveform and compressive sensing," *IEEE Transactions on Image Processing*, Vol. 26, No. 10, 5043–5056, 2017.
22. Fan, H., L. Ren, E. Mao, and Q. Liu, "A high-precision method of phase-derived velocity measurement and its application in motion compensation of ISAR imaging," *IEEE Transactions on Geoscience and Remote Sensing*, Vol. 56, No. 1, 60–77, 2018.
23. Chen, Y., et al., "An adaptive ISAR-imaging-considered task scheduling algorithm for multi-function phased array radars," *IEEE Transactions on Signal Processing*, Vol. 63, No. 19, 5096–5110, 2015.
24. Xiong, J., W. Wang, and K. Gao, "FDA-MIMO radar range-angle estimation: CRLB, MSE, and resolution analysis," *IEEE Transactions on Aerospace and Electronic Systems*, Vol. 54, No. 1, 284–294, 2018.
25. Xu, J., G. Liao, S. Zhu, L. Huang, and H. C. So, "Joint range and angle estimation using MIMO radar with frequency diverse array," *IEEE Transactions on Signal Processing*, Vol. 63, No. 13, 3396–3410, 2015.
26. Ma, Y., P. Wei, and H. Zhang, "General focusing beamformer for FDA: Mathematical model and resolution analysis," *IEEE Transactions on Antennas and Propagation*, Vol. 67, No. 5, 089–3100, 2019.
27. Donoho, D. L., "Compressed sensing," *IEEE Transactions on Information Theory*, Vol. 52, No. 4, 1289–1306, 2006.
28. Herman, M. A. and T. Strohmer, "High-resolution radar via compressed sensing," *IEEE Transactions on Signal Processing*, Vol. 57, No. 6, 2275–2284, 2009.
29. Potter, L. C., et al., "Sparsity and compressed sensing in radar imaging," *Proceedings of the IEEE*, Vol. 98, No. 6, 1006–1020, 2010.
30. Rong, J., Y. Wang, and T. Han, "Iterative optimization-based ISAR imaging with sparse aperture and its application in interferometric ISAR imaging," *IEEE Sensors Journal*, Vol. 19, No. 19, 8681–8693, 2019.
31. Elad, M., "Optimized projections for compressed sensing," *IEEE Transactions on Signal Processing*, Vol. 55, No. 12, 5695–5702, 2007.